Energy Conversion from Heat to Electricity by Highly Reversible Phase-Transforming Ferroelectrics

Chenbo Zhang,[1,2] Zhuohui Zeng,[1] Zeyuan Zhu,[1] Nobumichi Tamura,[3] and Xian Chen[1,*]

[1] *Department of Mechanical and Aerospace Engineering, Hong Kong University of Science and Technology, Clear Water Bay, Hong Kong*

[2] *HKUST Jockey Club Institute for Advanced Study, Hong Kong University of Science and Technology, Clear Water Bay, Hong Kong*

[3] *Advanced Light Source, Lawrence Berkeley National Laboratory, California 94720, USA*

(Received 10 June 2021; revised 22 July 2021; accepted 16 August 2021; published 31 August 2021)

The search for performant multiferroic materials has attracted general research interest in energy science as they have been increasingly exploited as the conversion media among thermal, electric, magnetic, and mechanical energies by using their temperature-dependent ferroic properties. Here we report a material development strategy that guides us to discover a reversible phase-transforming ferroelectric material exhibiting enduring energy harvesting from small temperature differences. The material satisfies the crystallographic compatibility condition between polar and nonpolar phases, which shows only 2.5 °C thermal hysteresis and a high figure of merit. It stably generates 15 μA of electricity in consecutive thermodynamic cycles in the absence of any bias fields. We demonstrate our device to consistently generate 6 $\mu A/cm^2$ current density near 100 °C over 540 complete phase transformation cycles without any electric and functional degradation. The energy-conversion device can light up an LED directly without attaching an external power source. This promising material candidate brings the low-grade waste-heat harvesting closer to a practical realization, e.g., small temperature fluctuations around the water boiling point can be considered as a clean energy source.

DOI: 10.1103/PhysRevApplied.16.024064

I. INTRODUCTION

Waste heat is inevitably generated from a plethora of processes, such as burning fuel, running computers, and solar radiation. The thermal energy that reaches temperatures of around 100 °C is abundant and has drastically increased in recent years from urban and industrial activities. As such, identifying methods to recycle and harvest waste heat is among the most pressing challenges in energy science.

Electrically polarized crystals naturally exhibit the pyroelectric effect: a change in temperature causes a change in its spontaneous electrical polarization. The earliest documented observation of the pyroelectric effect in stones such as tourmaline dates back to ancient Greece [1]. Since the 1960s, pyroelectric materials have attracted profound attention owing to their suitability for thermal sensing and thermal imaging [2,3]. Later, some theoretical models were proposed by Olsen, Evans, and Drummond to explore the heat-to-electricity conversion when utilizing these materials as the dielectric layer in capacitors, called dielectric power converters (DPCs) [4–6]. Their work underlies the thermodynamics of energy conversion by pyroelectric effect. Since then, this idea has been popularized as an important energy-harvesting approach for recycling low-grade waste heat, which was demonstrated in relaxor ferroelectrics [5,7,8] by the electric Ericsson cycle [6]. The pyroelectric current is produced in the isoelectric processes when the system is heated and cooled under alternative applied voltages. In Olsen's early demonstration [6], the pyroelectric converter was operated at 200 and 700 V in a temperature range from 140 to 160 °C. In Olsen's design, a drawback is the risk of applying high dc voltages during energy-conversion cycles. As the nanofabrication technologies flourished, the Olsen cycles have been realized in thin-film devices [9–12]. The applied bias voltage between two isoelectric processes of the Ericsson cycle is reduced to 2 and 8 V for thin-film pyroelectric capacitors [12,13]. A main problem of these latest devices is the confusion regarding where the electricity comes from. When an external electric source is attached during energy conversion, the pyroelectric current and the current caused by switching the external voltage are both collected in the circuit across the same load resistor. In some

*xianchen@ust.hk

designs of pyroelectric converters, the electric energies generated from the thermal fluctuations and from the electric field alternation are both accounted for as the harvest energy [12].

In the absent of applied electric bias field, the pyroelectric effect becomes very weak in common relaxor thin films, e.g., 0.055 $\mu C/(cm^2\,K)$ in PMN–0.32PT within the working temperature range for energy conversion [12]. This is one of the obstacles preventing pyroelectric energy conversion from achieving broad commercialization. Recent advances in innovative thermal management [12,14] and exquisite nanodevices [10,13,15] have pushed the device performance toward its current limit, that is, up to several hundreds of nanoamperes [10–13,15]. However, the ambient thermal fluctuations in nature can never reach the heating and cooling frequencies modeled in some reported devices [12,13]. This field urgently calls for more suitable materials to intrinsically improve the multiferroic thermal response.

II. MATERIAL DEVELOPMENT STRATEGIES

In relaxor ferroelectrics, the pyroelectric effect is characterized by the pyroelectric coefficient defined as dP/dT, where P is the spontaneous polarization and T is the temperature. Conventionally, searching for a large pyroelectric coefficient underlies the material design strategy. Therefore, it is common to utilize the lead-based ferroelectrics such as PZT and PMN-PT [7,8,12]. When a sharp phase transformation between polar and nonpolar structures occurs, the sudden drop in polarization within quite a narrow temperature interval gives rise to a singular dP/dT value. The phase transformations of barium titanate–based ferroelectrics belong to this case, whose transition temperature is around 120 °C. Compared with the relaxor ferroelectrics, the first-order phase-transforming barium titanate–based ferroelectrics are more suitable for the conversion from heat to electricity, especially in the low-grade temperature regime. As there is no spontaneous polarization in the cubic phase, we no longer use the terminology of pyroelectric energy conversion for the heat-to-electricity conversion by first-order phase transformation in this paper. We continue using the pyroelectric coefficient defined as dP/dT to express the temperature-dependent polarization variation, but dP/dT is a function of temperature, which becomes singular at the phase-transition temperature. As an example, the single-crystal $BaTiO_3$ undergoes a first-order phase transformation from tetragonal to cubic, the dP/dT of which at the transition temperature is calculated as $\Delta P_r/\Delta T \approx 1\ \mu C/cm^2\,K$ from experimental measurements [16]. That is about double the highest dP/dT reported in a lead-based relaxor PMN-0.32PT single crystal along the [111] polar axis at its transition temperature (180 °C) [17]. Note that all reported working temperatures of relaxor pyroelectric energy conversion are below 160 °C (i.e., within a single-phase regime), which means that relaxor devices are operated under much lower performance for energy conversion [10–12].

Utilizing the first-order phase transformation, people have indeed demonstrated promising energy-conversion performance using single-crystal $BaTiO_3$ by a ±5 °C temperature fluctuation near the transition temperature [18]. Reserved energies are more abundant in small thermal fluctuations than in a static temperature gradient. These rich thermal energies mainly oscillate at a rate of approximately 2 °C/s (0.5 Hz) around 100 °C from boiling water, running computers, and industrial waste heat [19]. Hence, finding the ferroelectric material undergoing first-order phase transformation at a proper temperature is a core strategy of material optimization. Compared with relaxor ferroelectrics, barium titanate and its sibling derivatives are the better candidates for energy conversion.

From energetic analysis, the cost of the energy conversion is the heat in the heating half cycle or the work required to cool the active material in the cooling half cycle, while the return is the change of polarization stored as the electrostatic energy. The ratio of pyroelectric coefficient to the heat capacity at a fixed bias field is a natural choice of figure of merit (FOM), which is, in fact, proposed for infrared sensors, such as $F_i = (1/c_E)dP/dT$, $F_v = (1/\epsilon_{33}c_E)dP/dT$ where c_E is the volume specific heat and ϵ_{33} is the permittivity along the polarized direction [20,21]. Both F_i (current) and F_v (voltage) represent the electric responsivity of a sensing device to the ambient temperature variations, not considering a thermodynamic cycle of energy harvesting. Another FOM for pyroelectric energy harvesting is derived from the analogy of the piezoelectric energy conversion, defined as $F_E = (1/\epsilon_{33})(dP/dT)^2$ [22]. Compared with the figures of merit F_v and F_i, the harvesting FOM, F_E, does not consider the heat capacity. Although it was widely used for device designs [12,23,24], the definition of F_E does not take into account the transient nature of heat transfer and the singularity of the transport properties in the vicinity of phase-transition temperature. It calls for a more suitable form of FOM considering the energy conversion from heat to electricity under a thermodynamic cycle that covers a first-order phase transformation.

Across a first-order phase transformation, both effective heat capacity and polarization undergo discontinuities in the vicinity of transition temperature, accompanied with a crystal structural change. The heat integrated over temperature is the latent heat ℓ, whereas the integrated dP/dT is the jump of polarization $[\![P]\!] = P_L - P_H$ where $P_{L,H}$ denote the polarization of the transforming material at temperatures below and above the transition temperature. Based on thermodynamic analysis of an energy-harvesting

cycle without application of a bias field, a different FOM is proposed [25]:

$$\mathrm{FOM} = \frac{\kappa[\![P]\!]}{\ell}, \tag{1}$$

where $\kappa = |dP/dT|_{\max}$ is the steepest slope of the polarization with respect to temperature, $[\![P]\!]$ is the change of polarization before and after phase transformation, and ℓ is the latent heat of phase transformation. The FOM in Eq. (1) considers an energy conversion in a temperature range covering a complete phase transformation from ferroelectric phase to paraelectric phase. It underlies the effect of intrinsic material properties on energy generation from heat to electricity caused by the abrupt drop of polarization. It rationalizes the searching of ferroelectric materials especially desirable for conversion from small temperature fluctuations to electricity by phase transformation. It is one of the key factors considered in this paper for material development.

To realize the cyclic transformations in a narrow temperature interval for energy conversion, the thermal hysteresis and functional degradation are unprecedented factors for the material design. It has been theorized that the transformation hysteresis and reversibility strongly rely on the crystallographic compatibility, that is, a tensor-metric condition on lattice parameters of both phases [26,27]. Mathematically, the primary criterion of compatibility is $\lambda_2 = 1$ where λ_2 is the middle eigenvalue of the transformation stretch tensor [27]. The value of λ_2 can be tuned by the lattice parameters of initial and final phases. It has been successfully used as a search index for low-hysteresis shape-memory alloys [28–31] and transforming oxides with enhanced structural reversibility [32–35]. Some recent discoveries have shown that ferroic properties such as electromagnetic [36], ferroelectric [35], and elasto/magneto caloric [37] are closely related to the crystallographic compatibility, and can be optimized when lattice parameters meet the $\lambda_2 = 1$ condition. As ferroic properties are keenly sensitive to crystal structures, searching for proper dopants to finely tune the lattice parameters of barium titanate is another important design strategy.

III. MATERIAL DEVELOPMENT

Considering the working temperature regime (about 100 °C), the nonlead toxicity, and the first-order phase transformation, we select three dopants Ca, Zr, and Ce to develop barium titanate–based ferroelectrics, named as tridoped BT. The reasons are as follows. The Ca addition at 5 at.% is to ensure a reversible tetragonal (ferroelectric) to cubic (paraelectric) transformation below 120 °C, according to the phase diagrams [38,39]. Preliminary studies [25,35,40] have shown that the addition of Zr increases the polarization jump across the phase transformation, potentially boosting the FOM. The charge leakage in ferroelectrics is unavoidable and nonnegligible, especially at elevated temperature [40–42]. This significantly hinders the long-lasting energy conversion performance owing to the electric degradation, discussed in Ref. [40]. Experiments [40,43] show that Ce is an effective dopant to reduce the charge leakage in a barium titanate system. Compared with $BaTiO_3$ and $Ba(Zr,Ti)O_3$ systems, only 1 at.% Ce doping can reduce the leakage current density by 1–3 orders of magnitude. The subtle lattice parameter adjustments can be achieved by tuning compositions of the dopants Zr and Ce within the range 0.1–1 at.%.

A. Synthesis and characterizations

A series of $Ba_{0.95}Ca_{0.05}Ti_{1-x-y}Zr_xCe_yO_3$ oxides are synthesized by solid-state reaction and densification process to obtain homogeneous polycrystalline rods of high density. The powders of $CaCO_3$ (Alfa Aesar, 99.5%), CeO_2 (Alfa Aesar, 99.9%), ZrO_2 (Sigma Aldrich, 99%), $BaCO_3$ (Alfa Aesar, 99.8%), and TiO_2 (Alfa Aesar, 99.8%) are weighed and well mixed according to the stoichiometric formulation $Ba_{0.95}Ca_{0.05}Ti_{1-x-y}Zr_xCe_yO_3$, for $(x,y) = (0.001, 0.005)$, $(0.005, 0.005)$, $(0.01, 0.005)$, $(0.01, 0.01)$, and $(0.01, 0.001)$. Then the powder mixture, which is milled by zirconia balls in a planetary ball miller at 630 rpm for 24 h, is dispersed in the ethanol solvent. The ball-milled solution is dried and calcined at 1000 °C for 10 h to obtain the tridoped barium titanate powder through solid-state reaction. Under a 30 MPa hydrostatic pressure at room temperature, the powder is cold-pressed for 30 min to form a rod-shaped green body with size 10 mm × ø6 mm. The sintering process is divided into two steps by a four-mirror infrared furnace (Quantum Design IRF11-001-00): (1) densification of feed and seed rods [40]; (2) grain-coarsening by floating-zone method [44,45]. The floating-zone synthesis is conducted as a presintering process by passing through the focal point of the four mirrors slowly with an axial speed of 3 mm/h and an angular speed of 3 rpm. The sintering temperature is around 1500 °C for both densification and grain-coarsening processes. With much less sintering time, all presintered rods are polycrystals with high densities; particularly, they are 5.375 g/cm^3, 5.493 g/cm^3, 5.451 g/cm^3, 5.335 g/cm^3, 5.443 g/cm^3 for $(x,y) = (0.001, 0.005)$, $(0.005, 0.005)$, $(0.01, 0.005)$, $(0.01, 0.01)$, and $(0.01, 0.001)$. The compositions of tridoped BT samples are characterized by the energy dispersive x-ray (EDX) spectroscopy analysis by JEOL 6390. The variation of the normalized intensity is characterized for elements Ba, Ti, O, Ca, Zr, and Ce along a 1.2-mm line on the surface for all samples. The atomic weight percentages are analyzed based on the spectra of the polycrystalline tridoped BT samples. Note that the absolute values of either counts or atomic percentages given by EDX spectroscopy are not sufficiently accurate to identify

the exact doping contents. The main purpose of EDX characterization is to examine the spatial homogeneity of the dopants and the compositional consistency with the nominal compositions. We confirm that the spatial variations are sufficiently small with respect to their mean values.

The temperature-dependent ferroic properties are characterized by the aixACCT TF2000E ferroelectric analyzer at a temperature step of 0.5 °C. At each of the temperature steps, we measure the polarization versus electric field curve under 10 Hz frequency shown as the inset of Fig. 1(a). The remnant polarization at zero field is recorded to plot the polarization-temperature curve. Note that under the real working condition for energy conversion, the zero-field polarization may not be fully achieved. Figures 1(a) and 1(b) show the temperature-dependent spontaneous polarization and corresponding $|dP/dT|$ of five nominal compositions, labeled as "Zrx Cey" for $(x, y) = (0.005, 0.005)$, $(0.001, 0.005)$, $(0.01, 0.005)$, $(0.01, 0.01)$, and $(0.01, 0.001)$. Note that the two compositional parameters (x, y) are tuned independently; we do not observe a systematic trend of property variations with regard to any of the specific tuning directions.

All of the tridoped BT show large $[\![P]\!]$ and steep dP/dT slopes within 100 to 120 °C, among which the Zr0.005 Ce0.005 specimen gives the largest $[\![P]\!] = 7.58\ \mu C/cm^2$ and $\kappa = 1.31\ \mu C/cm^2\,K$. The thermal analysis is conducted by differential scanning calorimetry (DSC) using TA Instruments DSC-250 in Fig. 1(c). The result reaffirms that they all undergo first-order phase transformations as big peaks of the heat flow are detected during heating and cooling through the transformation temperatures. Table I summarizes the ferroelectric properties and FOM defined in Eq. (1) for these five samples compared with typical ferroelectric poly/single crystals reported in literature. Among them, Zr0.005 Ce0.005 gives the largest FOM, that is, 1.52 $\mu C^2/J\,cm\,K$ in polycrystal and 3.55 $\mu C^2/J\,cm\,K$ in single crystal.

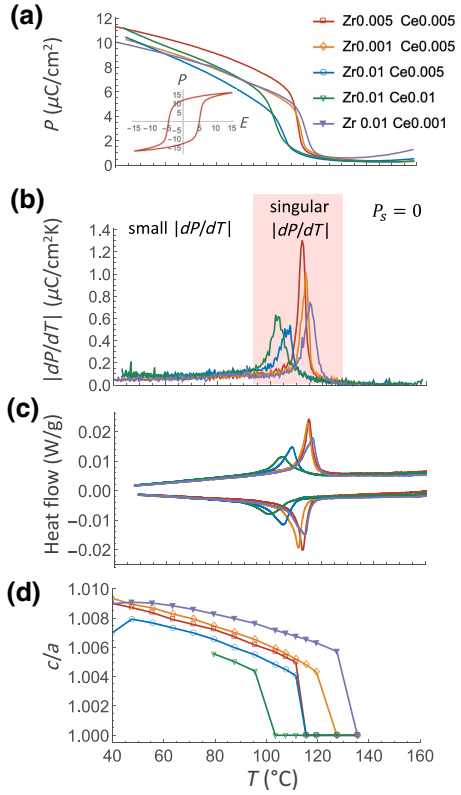

FIG. 1. Ferroelectric, thermal, and structural characterizations of first-order phase transformation in polycrystalline tridoped barium titanate crystals. (a),(b) Temperature-dependent polarization and absolute value of pyroelectric coefficient dP/dT. (c) Thermal analysis of reversible phase transformations by DSC. (d) Temperature-dependent c/a ratio by neutron diffraction experiments. The inset of (a) is the polarization versus electric field of Zr0.005 Ce0.005 at 40 °C.

B. Correlation between the transport properties and crystallographic compatibility

The lattice parameters are measured by neutron diffraction at the general-purpose powder diffractometer (GPPD) beamline at the China Spallation Neutron Source, suitable for structural characterization of large bulk samples [47]. We conduct the temperature-varying diffraction experiments for densified polycrystalline rods (ø5 × 50 mm^3) from 40 to 140 °C at a step of 10 °C per scan. Before each of the θ-2θ scans, the bulk sample is set in an isothermal environment until the temperature reading is stable. The cubic (high-temperature phase) and tetragonal (low-temperature phase) lattice parameters are refined by $Pm\bar{3}m$ and $P4mm$ space groups by the Rietveld refinement using GSAS suite with EXPGUI [48]. The same procedure is conducted for the other four bulk samples in different compositions. The tetragonality defined as the c/a ratio is presented in Fig. 1(d) where the lattice parameters are refined based on the diffraction patterns at different temperatures (e.g., Fig. 2).

Stark discontinuity of tetragonality exists in all compositions [Fig. 1(d)], which provides evidence that the first-order structural phase transformation is consistent with the abrupt jump of polarization [Fig. 1(a)], the singularity of pyroelectric coefficient [Fig. 1(b)], and the big heat flow peaks in DSC measurements [Fig. 1(c)].

The transformation stretch tensor is determined as a homogeneous linear transformation that deforms a unit cell of high-symmetry lattice to the primitive unit cell of low-symmetry lattice [49]. This has been theorized and experimentally verified for crystalline solids undergoing martensitic transformations [28–36]. In the case of phase transformation between tetragonal and cubic phases of our material system, the three cubic axes of paraelectric phase are deformed to the a, b, and c axes of the tetragonal

TABLE I. Summary of energy-conversion properties and compatibility of samples developed in this work and important ferroelectrics reported in literature. The $[\![P]\!]$ is calculated for a 20 °C temperature interval near 100 °C.

Materials	$[\![P]\!]$ (μC/cm^2)	κ (μC/cm^{2}K)	ℓ (J/cm^3)	FOM (μC^2/J cm K)	Temp. range (°C)
Zr0.005 Ce0.005	7.58	1.31	6.55	1.52	105–125
Zr0.005 Ce0.005 sc	11.68	1.93	6.34	3.55	
Zr0.001 Ce0.005	6.11	1.02	6.20	1.00	105–125
Zr0.01 Ce0.005	5.58	0.54	5.33	0.57	100–120
Zr0.01 Ce0.01	6.48	0.63	5.67	0.72	100–120
Zr0.01 Ce0.001	5.81	0.74	6.53	0.66	105–125
Zr0.01 Ce0.001 coarse	6.27	1.01	6.28	1.01	
$BaTiO_3$ sc [16]	6.0	1.0	5.69	1.05	115–135
$Ba(Ti, Zr_{0.017})O_3$ poly [35]	2.5	0.58	$\sim$ 5 to 6	0.24 to 0.29	120–140
PMN–0.32PT sc	1.56 [17]	0.08 [17]	7.5[a]	0.014	100–125
PMN–PT thin film		0.055 [12]		...[b]	100–120

[b]There is no reported thermal analysis of this system.
[a]The transferred heat is calculated as $c_E \Delta T$ for specific heat $c_E = 0.3$ J/cm^3 K [46].

ferroelectric phase. The transformation stretch tensor is calculated as

$$\mathbf{U} = \begin{bmatrix} \frac{a}{a_0} & 0 & 0 \\ 0 & \frac{a}{a_0} & 0 \\ 0 & 0 & \frac{c}{a_0} \end{bmatrix}. \quad (2)$$

where a_0 is the lattice parameter of cubic phase, a, c are the lattice parameters of tetragonal ferroelectric phase. The primary compatibility indexer λ_2 is calculated as the middle eigenvalue of $\mathbf{U}$, directly computed as $\lambda_2 = a/a_0$. It has been theorized that the distance of λ_2 to 1 underlies the height of the energy barrier of a symmetry-breaking transformation [50]. It has been shown in many phase-transforming systems that the thermal hysteresis and reversibility of a solid-phase transformation strongly relies on the compatibility condition [26,28–30].

The thermal hysteresis is calculated as $\Delta T = (A_s + A_f - M_s - M_f)/2$, in which the austenite start/finish A_s/A_f and martensite start/finish M_s/M_f temperatures are determined as the onsets of the heat emission/absorption peaks in Fig. 1(c). In our material system, the composition

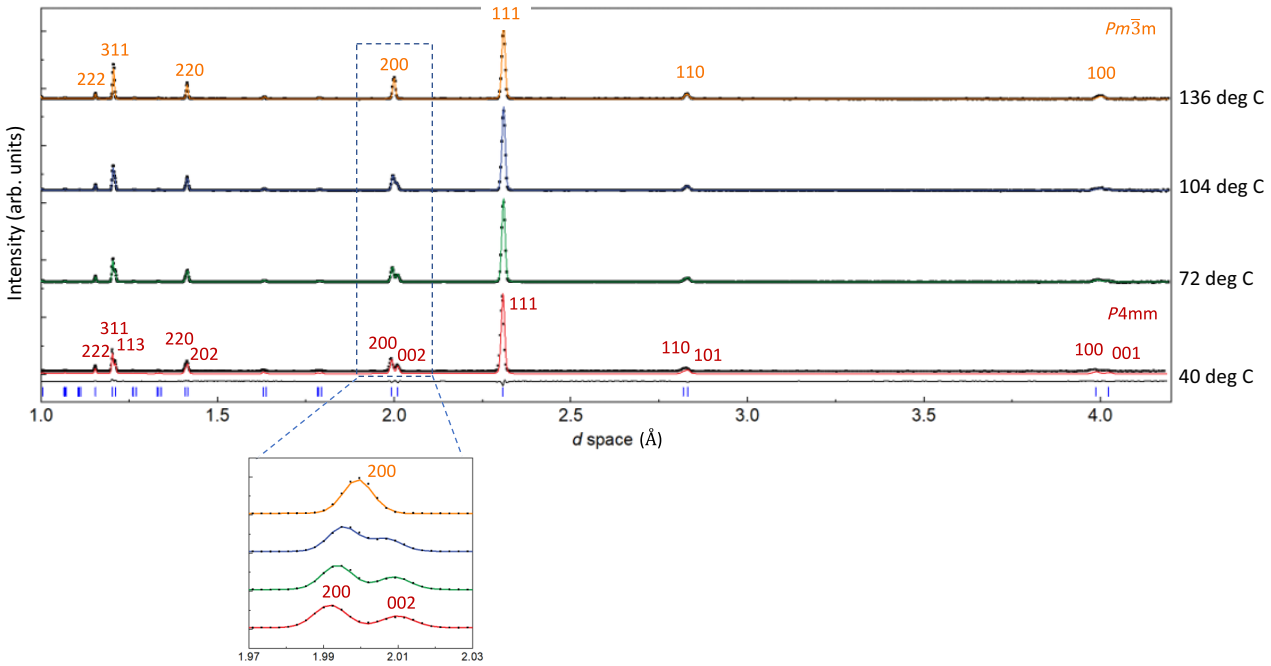

FIG. 2. Neutron diffraction pattern of Zr0.005 Ce0.005 polycrystalline bulk sample at elevated temperatures from 40 to 140 °C indexed by $Pm\bar{3}m$ (cubic) and $P4mm$ (tetragonal) symmetries.

Zr0.005 Ce0.005 shows the smallest thermal hysteresis, 2.5 °C corresponding to the largest FOM among all tested compositions in Figs. 3(a) and 3(b), meanwhile it satisfies closely the compatibility condition as indicated in Fig. 3(c) corresponding to the structural parameters and compatibility indexers listed in Table II. Our observation in tridoped BT system implies a strong correlation between the compatibility indexer λ_2 and the change of polarization across the first-order phase transformation. The maximum FOM resonates with the minimum of hysteresis corresponding to the most compatible first-order phase transformation. The large FOM given by the composition Zr0.005 Ce0.005 makes it an ideal material candidate for the heat-to-electricity conversion demonstration.

C. Steep polarization jump at phase transformation in single crystal

For demonstration, it is critical to fabricate a high-quality capacitor with the capacitance sensitive to temperature variation within the thermal fluctuation range. A previous energy conversion attempt [18] by first-order phase transformation evidently suggests that the single $BaTiO_3$ crystal can magnificently enhance the performance of the device. We adopt the floating-zone method, an economic way to grow single crystals, to coarsen the grains in two fine-grained polycrystals: Zr0.01 Ce0.001 and Zr0.005 Ce0.005. We select two of the polycrystalline rods as the seed and feed aligned vertically for the crystal growth by the floating-zone method at a growth speed of 10 mm/h and relative angular speed of 25 rpm at an increasing lamp power. The molten zone is created and monitored throughout the entire growth period. Finally, the as-grown rod is solidified as the furnace cools down. The rod is sliced along the growth direction followed by a mechanical polish. The size of the ceramic slices is about $19.5 \times 5.5 \times 0.4$ mm^3. After mechanical polishing, both the Zr0.01 Ce0.001 and Zr0.005 Ce0.005 slices become semitransparent. We use the dual beam-shear differential interference microscope to observe the grain boundaries and morphology, and the x-ray microdiffraction probe to quantitatively measure the orientation distribution of the single/coarse-grain bulks. Compared with the grain morphology of polycrystalline specimen in Fig. 4(a), the quantitative microstructure of the as-grown crystals is presented in Figs. 4(b) and 4(c) analyzed by synchrotron x-ray microdiffraction scans, characterized at Advanced Light Source, Beamline 12.3.2 at Lawrence Berkeley National Lab.

As we use polycrystal seeds for the floating-zone process, the cutting process of the as-grown rod is done without acknowledgment of orientation information. The microstructure of the polycrystalline specimen is similar among all compositions, showing equiaxed grains with sizes of 10 μm. The twin structures are clearly seen in some of the grains. In contrast, the orientation maps of as-grown Zr0.005 Ce0.005 and Zr0.01 Ce0.001 exhibit strong textures. Clearly, the Zr0.005 Ce0.005 plate is a single crystal of millimeter size, while the Zr0.01 Ce0.001 plate is a coarse-grained crystal having multiple millimeter grains. The surface normal of Zr0.005 Ce0.005 is measured as $[0.9, 1.5, 1.8]$ written in the crystal basis.

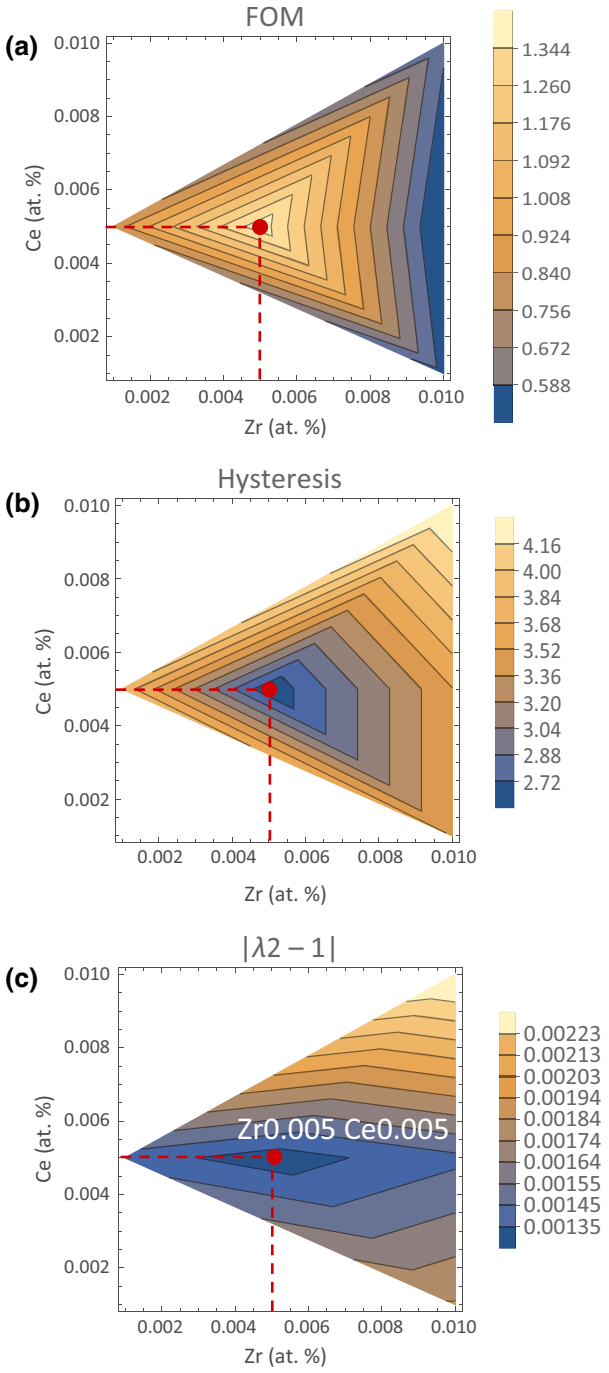

FIG. 3. Contours of (a) FOM, (b) thermal hysteresis, and (c) compatibility condition in two-dimensional composition space interpreted from experimental data by linear interpolation.

TABLE II. Lattice parameters of polycrystalline tridoped BT samples measured by neutron diffraction corresponding to their compatibility indexer λ_2.

Materials	a_0(Å) after T_c	a(Å) before T_c	c(Å) before T_c	λ_2
Zr0.005 Ce0.005	3.99908	3.99388	4.01373	0.9987
Zr0.001 Ce0.005	4.00345	3.99744	4.01506	0.9985
Zr0.01 Ce0.005	4.00716	4.00075	4.01703	0.9984
Zr0.01 Ce0.01	4.01088	4.00125	4.01890	0.9976
Zr0.01 Ce0.001	4.00302	3.99581	4.01885	0.9982

Although it is not perfectly aligned with the polar axis [001], its $[\![P]\!]$ reaches 11.7 μC/cm^2, corresponding to $\kappa = 1.93$ μC/cm^2 K, shown in Figs. 5(a) and 5(b).

These values are about twice the largest reported values in a single-crystal $BaTiO_3$ aligned with its polar axis [16]. As the goal of energy conversion is to harvest low-grade waste heat, we consider 20 °C temperature difference near 100 °C to benchmark the ferroelectrics in our work and literature in Table I. A Zr0.005 Ce0.005 single crystal exhibits by far the largest polarization jump and pyroelectric coefficient. The coarsened Zr0.01 Ce0.001 crystal also exhibits some degree of improvement in $[\![P]\!]$ compared with its fine-grained polycrystal counterpart. Figure 5 compares the ferroic properties near the transformation temperature between the single/coarsened crystals and their polycrystalline form. First, we confirm that both transform at the same temperature despite whether they are single crystals or polycrystals. Second, both polarization jump and pyroelectric coefficient at transition temperature are magnified significantly. The leakage current densities are measured as 0.064 μA/cm^2 for Zr0.005 Ce0.005, and 0.337 μA/cm^2 for Zr0.01 Ce0.001 under the application of 3 kV/cm electric field.

D. Energy-conversion demonstration for long thermal cycles

We make planar capacitors using the Zr0.005 Ce0.005 single crystal and the Zr0.01 Ce0.001 coarse-grained slices by using the conductive silver paste as the electrodes. The dimensions of the transforming capacitors are 16.5 mm^2 × 0.46 mm for Zr0.005 Ce0.005 single-crystal capacitor and

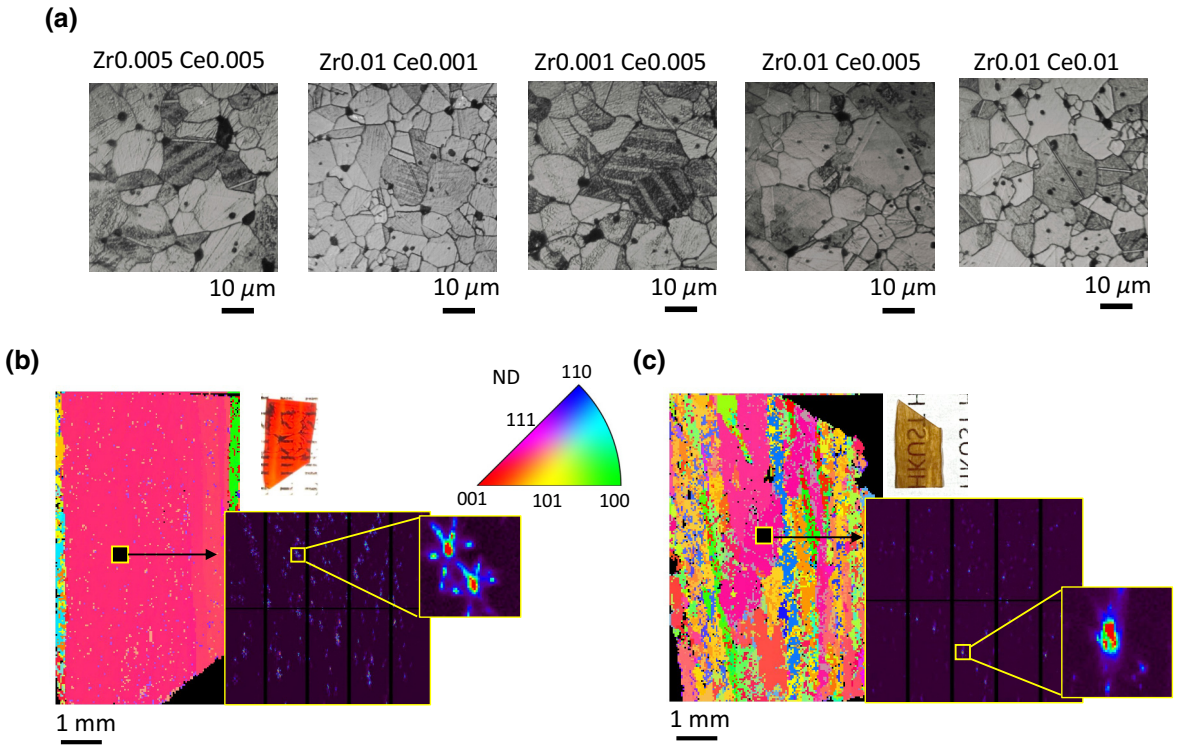

FIG. 4. The grain morphology of (a) polycrystalline $Ba_{0.95}Ca_{0.05}TiZr_xCe_yO_3$. Orientation maps by synchrotron Laue microdiffraction for (b) Zr0.005 Ce0.005 and (c) Zr0.01 Ce0.001 grown by floating-zone method. The color map indicates the orientation of normal direction (ND) of the surface.

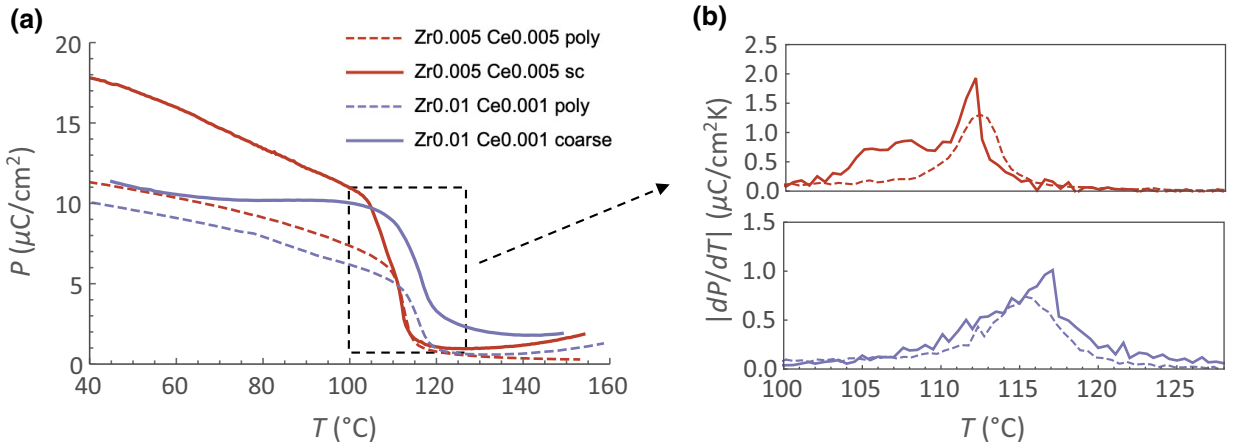

FIG. 5. Ferroic properties of Zr0.005 Ce0.005 single crystal and Zr0.01 Ce0.001 coarse-grain crystal. (a) Temperature-dependent polarization and (b) absolute value of dP/dT in a zoomed temperature range between 100 and 130 °C.

25.28 mm^2 × 0.44 mm for Zr0.01 Ce0.001 coarse-grain capacitor. The demonstration apparatus is illustrated in Fig. 6, which is analyzed by a thermodynamic model with complete removal of external bias field during energy conversion [25,40].

A nontransforming capacitor (10 μF, from RS Components Ltd.) used as a charge reservoir is connected to the phase-transforming capacitor. Both are grounded and bridged via a resistor (1 MΩ, from RS Components Ltd.) to measure the electric signal generated by first-order phase transformation of the active material. The capacitors are initially charged up to hold sufficient initial charges, then detached from the external power source throughout the heating and cooling cycles. We use a custom-made thermal stage whose heating/cooling rates mimic the natural thermal fluctuations from waste heat between 95 and 125 °C, oscillating at a frequency of about 0.05 Hz. The charges flow back and forth between the transforming and nontransforming capacitors driven by the ferro-to-paraelectric phase transformation. We measure the electric voltage V using an Agilent 34970A data acquisition module on the load resistor R in Fig. 6(b) to calculate the pyroelectric current as V/R, in short pyro-current [51]. Note that the voltage signal can be magnified by using a large resistor, but it does not represent a true improvement of energy conversion performance, as the load resistance is given in practical applications. Hence, pyro-current is a more proper meter in our energy-conversion setup.

Figure 7(a) demonstrates continuous generation of electricity of more than 3 h by the Zr0.005 Ce0.005 capacitor, compared with the Zr0.01 Ce0.001 capacitor over hundreds of transformation cycles. The current is generated when temperature passes the phase-transformation temperatures during both heating and cooling processes, in Figs. 7(b) and 7(c). It verifies that the electric energy is purely converted from temperature differences, not from the discharge of the external battery. The pyro-current generated by the Zr0.005 Ce0.005 single-crystal capacitor reaches up to 1 μA lasting over 500 transformation cycles with continuous energy output of 9.87 kJ/m^3. For

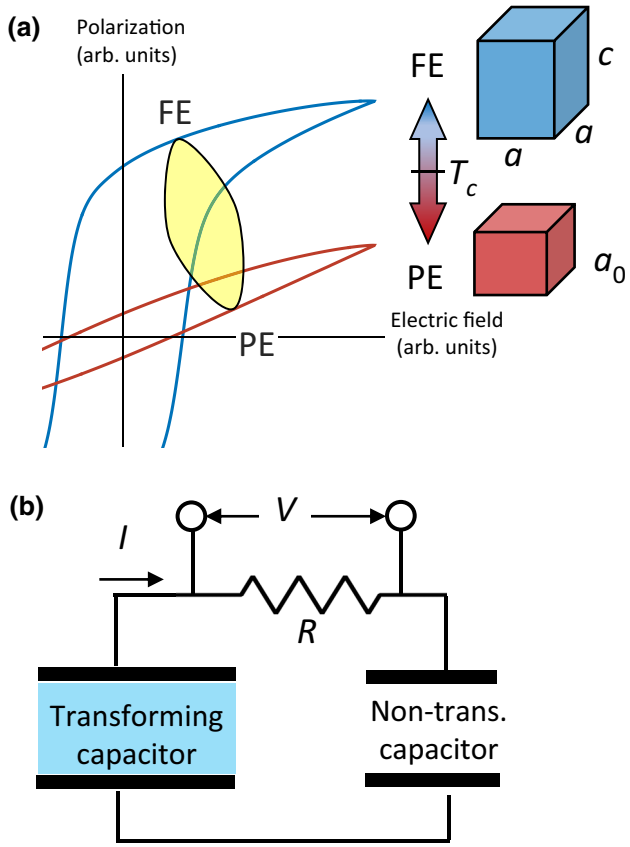

FIG. 6. (a) Schematic polarization-field curves of tetragonal ferroelectric phase (blue) and cubic paraelectric phase (red). The yellow area demonstrates the thermodynamic cycle of the process without application of external bias electric field. (b) Battery detached setup of the transforming capacitor with polarization jump between ferroelectric and paraelectric phases.

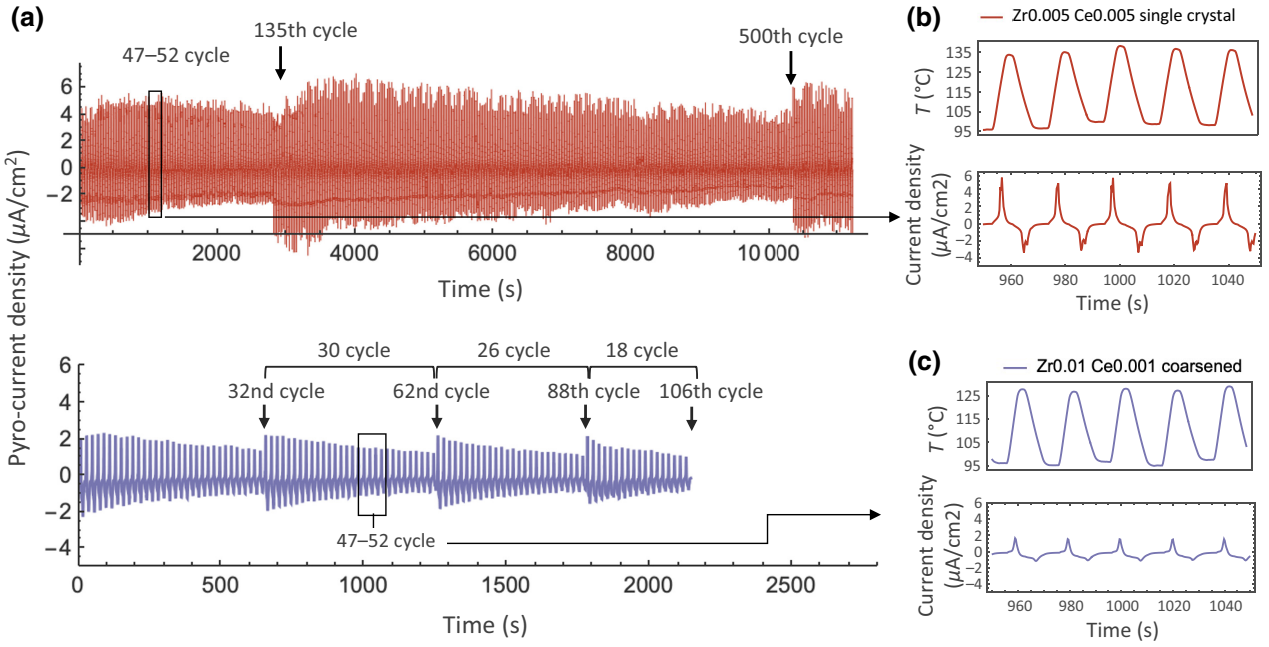

FIG. 7. Energy conversion by phase-transforming ferroelectric crystals. (a) Pyro-current density generated by the Zr0.005 Ce0.005 single-crystal capacitor (red) and the Zr0.01 Ce0.001 coarse-grained capacitor (blue) over hundreds of transformation cycles. (b),(c) Pyroelectric current density of 47 to 52 cycles corresponding to the applied temperature profiles.

the Zr0.01 Ce0.001 coarse-grained capacitor, the pyro-current generated in the first few cycles is 0.5 μA. To benchmark capacitors with different areas, we calculate the current density, that is, current per area: 6 μA/cm^2 for Zr0.005 Ce0.005 and 2 μA/cm^2 for Zr0.01 Ce0.001. These results are aligned with our theoretical prediction by FOM for material development. This confirms that the FOM in Eq. (1) is a good performance indexer of energy conversion by first-order phase transformation.

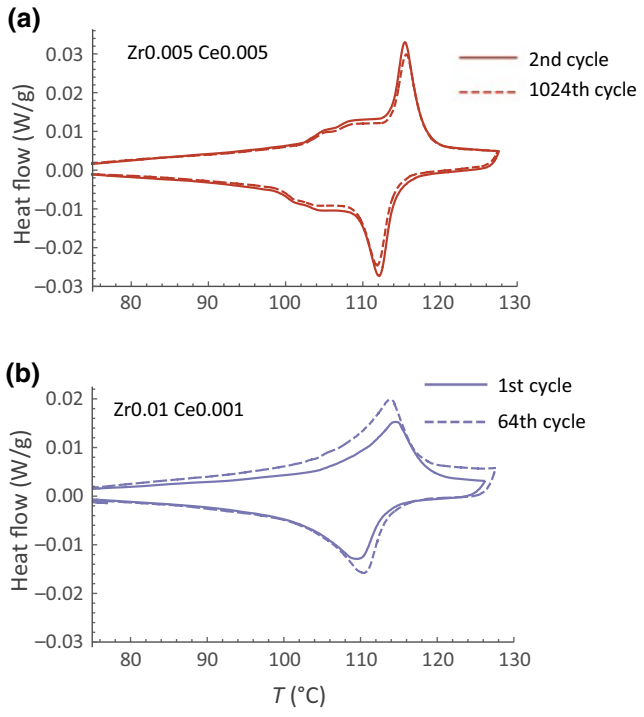

FIG. 8. Differential scanning calorimetry measurement of (a) Zr0.005 Ce0.005 single-crystal plate (red) and (b) Zr0.01 Ce0.001 coarse-grained plate (blue) at initial and final thermal cycles.

As the Zr0.01 Ce0.001 capacitor exhibits larger electric leakage, it suffers electric degradation [40] over a period of energy conversion process. Consequently, a recharge is necessary after several thermodynamics cycles. We use the half-life, defined as the number of cycles from initial charge state to the state that loses 50% of charge, to evaluate whether the energy-conversion device needs a pack of recharge. The energy cost in a full pack of recharge can be estimated as $CV_0^2/8$ where C is the capacitance and V_0 is the voltage given by the initialization for the transforming capacitor. It requires four full recharges to maintain a decent power output at the 106th cycle, labeled in the bottom panel of Fig. 7(a). In contrast, the Zr0.005 Ce0.005 capacitor has no visible electric degradation during the first 135 cycles. Although it does not reach the half-life, we conduct a pack of recharge before the 136th cycle for comparison. After such a recharge, the generation of pyro-current sustains for 365 cycles until the second recharge at its half-life, corresponding to the top panel of Fig. 7(a). An important observation is that the number of cycles in each half-life in the Zr0.01 Ce0.001 capacitor keeps shrinking, which implies a functional degradation of the transforming material.

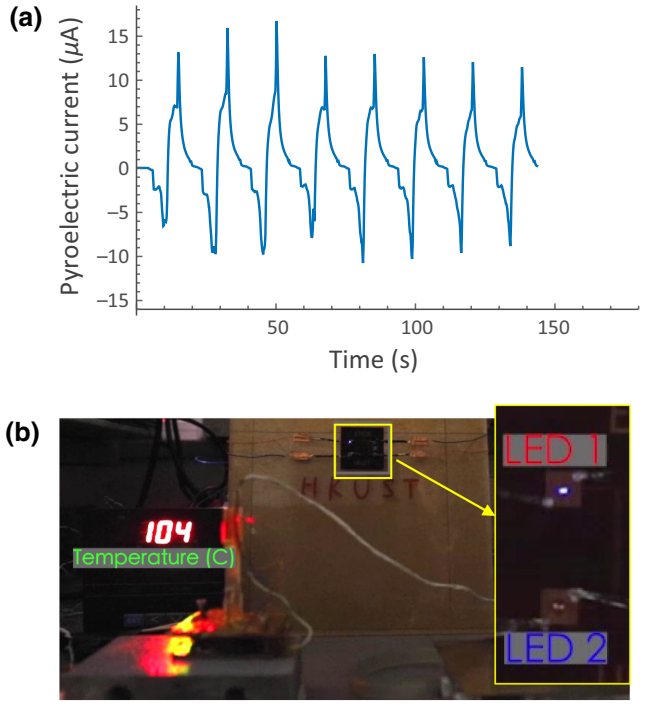

FIG. 9. (a) Generated current by a grid of phase-transforming Zr0.005 Ce0.005 capacitors connected in parallel under ±20 °C temperature differences around 110 °C. (b) The demonstration to light up an LED light during heating.

The Zr0.005 Ce0.005 capacitor with λ_2 much closer to 1 exhibits high reversibility for cyclic phase transformation. The thermal reversibility of these two capacitors is examined by cyclic DSC experiments, shown in Fig. 8. The Zr0.005 Ce0.005 capacitor after 1024 thermal cycles shows no migration of transformation temperature (115 °C), nor the magnification of the hysteresis (2.7 °C) compared with the hysteresis in the first cycle (2.5 °C). This coincides with the satisfaction of the compatibility condition $\lambda_2 = 1$ [Figs. 3(b) and 3(c)].

We cut 38 pieces of similar size from several rods of Zr0.005 Ce0.005 synthesized by the same method and assemble them in parallel in our demonstration setup. The total area is 2344.88 mm^2, and the mean thickness is about 0.4 mm. In this setting, we use a bigger reference capacitor (140 μF) connected to the same load resistor. All capacitors are initially charged up to have 1.2 kV/cm electric field inside, then the external power is completely disconnected to begin the energy-conversion cycles. The grid of energy-conversion devices generates stably 15 μA electric current in consecutive cycles, in Fig. 9(a). Thanks to the phase stability, low hysteresis, and large pyro-current generated per cycle, the Zr0.005 Ce0.005 capacitor can directly light up an LED during both heating [Fig. 9(b)] and cooling processes through phase transformation (see Movie S1 in the Supplemental Material [52]).

IV. CONCLUSIONS

Enabling waste-heat harvesting, particularly in relatively low-temperature regimes, is an interdisciplinary and multifaceted grand challenge in energy science. Core material development is undoubtedly one of the key imperatives. Rational FOM, phase compatibility, and leakage suppression underlie essential design strategy for materials with minimal functional degradation and high energy-conversion performance. Aspects such as manageable temperature cycling, efficient heat transfer, collecting intermittent electricity, and compact-device packaging still call for breakthrough improvement; this work is a substantial step forward from the aspect of material development toward the practical realization of pyroelectric energy conversion. When the research focus in this field shifts from device design to material development, more fundamental studies are needed, especially the investigation of the domain structures and the corresponding influence on the ferroelectric property of the tetragonal phase.

ACKNOWLEDGMENTS

The authors appreciate fruitful discussion with Dr. Yintao Song during the preparation of the manuscript. Lunhua He and Sihao Deng are acknowledged for their help on the neutron powder diffraction experiments which were performed at GPPD of the China Spallation Neutron Source (CSNS), Dongguan, China. C. Z., Z. Zeng, Z. Zhu and X. C. are grateful for financial support under GRF Grants No. 16201118 and No. 16201019, CRF Grant No. C6016-20G from the HK Research Grants Council and the Bridge Gap Fund, BGF.009.19/20, from the HKUST Technology Transfer Center. The experiment is supported by Electronic Packaging Lab in HKUST. This research used BL12.3.2 which is a resource of the Advanced Light Source, a US DOE Office of Science User Facility under Contract No. DE-AC02-05CH11231.

[1] S. B. Lang, Pyroelectricity: A 2300-year history, Ferroelectrics **7**, 231 (1974).
[2] R. Whatmore, Pyroelectric devices and materials, Rep. Prog. Phys. **49**, 1335 (1986).
[3] S. Bauer and B. Ploss, A simple technique to interface pyroelectric materials with silicon substrates for infrared detection, Ferroelectr., Lett. Sect. **9**, 155 (1989).
[4] J. Drummond, V. Fargo, J. Ream, J. Briscoe, and D. Brown, in *14th Intersociety Energy Conversion Engineering Conference* (American Chemical Society, Boston, Massachusetts, 1979), Vol. 2, p. 1819.
[5] R. B. Olsen and D. Evans, Pyroelectric energy conversion: Hysteresis loss and temperature sensitivity of a ferroelectric material, J. Appl. Phys. **54**, 5941 (1983).
[6] R. B. Olsen, D. A. Bruno, and J. M. Briscoe, Pyroelectric conversion cycles, J. Appl. Phys. **58**, 4709 (1985).

[7] G. Sebald, S. Pruvost, and D. Guyomar, Energy harvesting based on Ericsson pyroelectric cycles in a relaxor ferroelectric ceramic, Smart Mater. Struct. **17**, 015012 (2008).

[8] G. Sebald, D. Guyomar, and A. Agbossou, On thermoelectric and pyroelectric energy harvesting, Smart Mater. Struct. **18**, 125006 (2009).

[9] A. Navid and L. Pilon, Pyroelectric energy harvesting using Olsen cycles in purified and porous poly (vinylidene fluoride-trifluoroethylene)[P(VDF-TrFE)] thin films, Smart Mater. Struct. **20**, 025012 (2011).

[10] Y. Yang, S. Wang, Y. Zhang, and Z. L. Wang, Pyroelectric nanogenerators for driving wireless sensors, Nano Lett. **12**, 6408 (2012).

[11] B. Bhatia, A. R. Damodaran, H. Cho, L. W. Martin, and W. P. King, High-frequency thermal-electrical cycles for pyroelectric energy conversion, J. Appl. Phys. **116**, 194509 (2014).

[12] S. Pandya, J. Wilbur, J. Kim, R. Gao, A. Dasgupta, C. Dames, and L. W. Martin, Pyroelectric energy conversion with large energy and power density in relaxor ferroelectric thin films, Nat. Mater. **17**, 432 (2018).

[13] A. P. Sharma, M. K. Behera, D. K. Pradhan, S. K. Pradhan, C. E. Bonner, and M. Bahoura, Lead-free relaxor-ferroelectric thin films for energy harvesting from low-grade waste-heat, Sci. Rep. **11**, 111 (2021).

[14] S. Pandya, J. D. Wilbur, B. Bhatia, A. R. Damodaran, C. Monachon, A. Dasgupta, W. P. King, C. Dames, and L. W. Martin, Direct Measurement of Pyroelectric and Electrocaloric Effects in Thin Films, Phys. Rev. Appl. **7**, 034025 (2017).

[15] Y. Ji, K. Zhang, Z. L. Wang, and Y. Yang, Piezo–pyro–photoelectric effects induced coupling enhancement of charge quantity in $BaTiO_3$ materials for simultaneously scavenging light and vibration energies, Energy Environ. Sci. **12**, 1231 (2019).

[16] X. Moya, E. Stern-Taulats, S. Crossley, D. González-Alonso, S. Kar-Narayan, A. Planes, L. Mañosa, and N. D. Mathur, Giant electrocaloric strength in single-crystal $BaTiO_3$, Adv. Mater. **25**, 1360 (2013).

[17] P. Kumar, S. Sharma, O. Thakur, C. Prakash, and T. Goel, Dielectric, piezoelectric and pyroelectric properties of PMN–PT (68: 32) system, Ceram. Int. **30**, 585 (2004).

[18] A. Bucsek, W. Nunn, B. Jalan, and R. D. James, Direct Conversion of Heat to Electricity Using First-Order Phase Transformations in Ferroelectrics, Phys. Rev. Appl. **12**, 034043 (2019).

[19] Y. Zhang, P. T. T. Phuong, E. Roake, H. Khanbareh, Y. Wang, S. Dunn, and C. Bowen, Thermal energy harvesting using pyroelectric-electrochemical coupling in ferroelectric materials, Joule **4**, 301 (2020).

[20] S. B. Lang and D. K. Das-Gupta, in *Handbook of advanced electronic and photonic materials and devices* (Elsevier, New York, 2001), p. 1.

[21] C. R. Bowen, J. Taylor, E. LeBoulbar, D. Zabek, A. Chauhan, and R. Vaish, Pyroelectric materials and devices for energy harvesting applications, Energy Environ. Sci. **7**, 3836 (2014).

[22] G. Sebald, L. Seveyrat, D. Guyomar, L. Lebrun, B. Guiffard, and S. Pruvost, Electrocaloric and pyroelectric properties of $0.75Pb(Mg_{1/3}Nb_{2/3})O_3$–$0.25PbTiO_3$ single crystals, J. Appl. Phys. **100**, 124112 (2006).

[23] G. Sebald, E. Lefeuvre, and D. Guyomar, Pyroelectric energy conversion: Optimization principles, IEEE Trans. Ultrason. Ferroelectr. Freq. Control **55**, 538 (2008).

[24] R. Mangalam, J. Agar, A. Damodaran, J. Karthik, and L. Martin, Improved pyroelectric figures of merit in compositionally graded $PbZr_{1-x}Ti_xO_3$ thin films, ACS Appl. Mater. Interfaces **5**, 13235 (2013).

[25] C. Zhang, Y. Song, M. Wegner, E. Quandt, and X. Chen, Power-Source-Free Analysis of Pyroelectric Energy Conversion, Phys. Rev. Appl. **12**, 014063 (2019).

[26] J. M. Ball and R. D. James, Fine phase mixtures as minimizers of energy, Arch. Ration. Mech. Anal. **100**, 13 (1987).

[27] X. Chen, V. Srivastava, V. Dabade, and R. D. James, Study of the cofactor conditions: Conditions of supercompatibility between phases, J. Mech. Phys. Solids **61**, 2566 (2013).

[28] J. Cui, Y. S. Chu, O. O. Famodu, Y. Furuya, J. Hattrick-Simpers, R. D. James, A. Ludwig, S. Thienhaus, M. Wuttig, Z. Zhang, and I. Takeuchi, Combinatorial search of thermoelastic shape-memory alloys with extremely small hysteresis width, Nat. Mater. **5**, 286 (2006).

[29] R. Zarnetta, R. Takahashi, M. L. Young, A. Savan, Y. Furuya, S. Thienhaus, B. Maaß, M. Rahim, J. Frenzel, H. Brunken, *et al.*, Identification of quaternary shape memory alloys with near-zero thermal hysteresis and unprecedented functional stability, Adv. Funct. Mater. **20**, 1917 (2010).

[30] Y. Song, X. Chen, V. Dabade, T. W. Shield, and R. D. James, Enhanced reversibility and unusual microstructure of a phase-transforming material, Nature **502**, 85 (2013).

[31] C. Chluba, W. Ge, R. L. de Miranda, J. Strobel, L. Kienle, E. Quandt, and M. Wuttig, Ultralow-fatigue shape memory alloy films, Science **348**, 1004 (2015).

[32] E. L. Pang, C. A. McCandler, and C. A. Schuh, Reduced cracking in polycrystalline ZrO_2-CeO_2 shape-memory ceramics by meeting the cofactor conditions, Acta Mater. **177**, 230 (2019).

[33] J. Jetter, H. Gu, H. Zhang, M. Wuttig, X. Chen, J. R. Greer, R. D. James, and E. Quandt, Tuning crystallographic compatibility to enhance shape memory in ceramics, Phys. Rev. Mater. **3**, 093603 (2019).

[34] Y. Liang, S. Lee, H. Yu, H. Zhang, Y. Liang, P. Zavalij, X. Chen, R. James, L. Bendersky, A. Davydov, *et al.*, Tuning the hysteresis of a metal-insulator transition via lattice compatibility, Nat. Commun. **11**, 3539 (2020).

[35] M. Wegner, H. Gu, R. D. James, and E. Quandt, Correlation between phase compatibility and efficient energy conversion in Zr-doped barium titanate, Sci. Rep. **10**, 3496 (2020).

[36] S. El-Khatib, K. P. Bhatti, V. Srivastava, R. James, and C. Leighton, Nanoscale magnetic phase competition throughout the Ni_{50-x} $Co_xMn_{40}Sn_{10}$ phase diagram: Insights from small-angle neutron scattering, Phys. Rev. Mater. **3**, 104413 (2019).

[37] D. Zhao, J. Liu, X. Chen, W. Sun, Y. Li, M. Zhang, Y. Shao, H. Zhang, and A. Yan, Giant caloric effect of low-hysteresis metamagnetic shape memory alloys with exceptional cyclic functionality, Acta Mater. **133**, 217 (2017).

[38] X. Liu, D. Wu, Z. Chen, B. Fang, J. Ding, X. Zhao, and H. Luo, Ferroelectric, dielectric and pyroelectric properties of Sr and Sn codoped BCZT lead free ceramics, Adv. Appl. Ceram. **114**, 436 (2015).

[39] I. Coondoo, N. Panwar, S. Krylova, A. Krylov, D. Alikin, S. K. Jakka, A. Turygin, V. Y. Shur, and A. L. Kholkin, Temperature-dependent Raman spectroscopy, domain morphology and photoluminescence studies in lead-free BCZT ceramic, Ceram. Int. **47**, 2828 (2021).

[40] C. Zhang, Z. Zeng, Z. Zhu, M. Karami, and X. Chen, Impact of Leakage for Electricity Generation by Pyroelectric Converter, Phys. Rev. Appl. **14**, 064079 (2020).

[41] B. Nagaraj, S. Aggarwal, T. Song, T. Sawhney, and R. Ramesh, Leakage current mechanisms in lead-based thin-film ferroelectric capacitors, Phys. Rev. B **59**, 16022 (1999).

[42] G. W. Pabst, L. W. Martin, Y.-H. Chu, and R. Ramesh, Leakage mechanisms in $BiFeO_3$ thin films, Appl. Phys. Lett. **90**, 072902 (2007).

[43] S. Wang, B. Cheng, C. Wang, S. Redfern, S. Dai, K. Jin, H. Lu, Y. Zhou, Z. Chen, and G. Yang, Influence of Ce doping on leakage current in $Ba_{0.5}Sr_{0.5}TiO_3$ films, J. Phys. D: Appl. Phys. **38**, 2253 (2005).

[44] A. M. Balbashov and S. K. Egorov, Apparatus for growth of single crystals of oxide compounds by floating zone melting with radiation heating, J. Cryst. Growth **52**, 498 (1981).

[45] S. Kimura and K. Kitamura, Floating zone crystal growth and phase equilibria: A review, J. Am. Ceram. Soc. **75**, 1440 (1992).

[46] S. T. Lau, C. Cheng, S. Choy, D. Lin, K. W. Kwok, and H. L. Chan, Lead-free ceramics for pyroelectric applications, J. Appl. Phys. **103**, 104105 (2008).

[47] J. Chen, L. Kang, H. Lu, P. Luo, F. Wang, and L. He, The general purpose powder diffractometer at CSNS, Phys. B: Condens. Matter **551**, 370 (2018).

[48] B. H. Toby, EXPGUI, a graphical user interface for GSAS, J. Appl. Crystallogr. **34**, 210 (2001).

[49] X. Chen, Y. Song, N. Tamura, and R. D. James, Determination of the stretch tensor for structural transformations, J. Mech. Phys. Solids **93**, 34 (2016).

[50] Z. Zhang, R. D. James, and S. Müller, Energy barriers and hysteresis in martensitic phase transformations, Acta Mater. **57**, 4332 (2009).

[51] For simplicity, we use the terminology *pyro-current* as the current generated purely by phase transformation.

[52] See Supplemental Material at http://link.aps.org/supplemental/10.1103/PhysRevApplied.16.024064 for Movie S1 that records the demonstration for lighting an LED directly by small thermal fluctuations near 100 °C without any chargeable batteries.